small structures
www.small-structures.com

Exceptional High-Performance Oxygen Transport Membrane and Comprehensive Study on Mass/Charge Transport Properties

Hohan Bae, Gyeong Duk Nam, Yeon Namgung, Kwangho Park, Jun-Young Park, José M. Serra, Jong Hoon Joo, and Sun-Ju Song**

This study focuses on mixed-conducting perovskite membranes for efficient oxygen supply, aiming to replace energy-intensive cryogenic distillation with a more practical alternative. A La and Nb co-doped $BaCoO_{3-\delta}$ perovskite is introduced, $Ba_{0.95}La_{0.05}Co_{0.8}Fe_{0.12}Nb_{0.08}O_{3-\delta}$ (BLCFN) with a record-breaking oxygen permeation flux, surpassing all known single-phase perovskite membranes. To elucidate its superior membrane performance, the mass/charge transport properties and equilibrium bulk properties are investigated and quantitative indicators ($D_O = 5.8 \times 10^{-6}\,cm^2\,s^{-1}$, $k_O = 1.0 \times 10^{-4}\,cm\,s^{-1}$, $\sigma_{ion} = 0.93\,S\,cm^{-1}$ at 900 °C) reveal fast diffusion and excellent surface gas-exchange kinetics. The oxygen permeability of 12.4 mL cm^{-2} min^{-1} and over 200 h of long-term stability is achieved in an air/He atmosphere at 900 °C. By presenting a material that demonstrates higher performance than $Ba_{0.5}Sr_{0.5}Co_{0.8}Fe_{0.2}O_{3-\delta}$ (BSCF), currently known for its highest permeability, it is believed that this marks a significant step toward innovative performance enhancement of perovskite oxide-based membranes.

1. Introduction

Since Teraoka et al.[1] proposed the oxygen transport membrane (OTM) concept, that utilizes mixed ionic-electronic conducting ceramic oxides, extensive research has been undertaken over the past decades. This research reveals the significant potential of OTM technology in various applications[2–5] such as oxygen production, partial oxidation of hydrocarbons, and gas reforming. By applying OTMs to high-temperature processes such as industrial boilers, biomass oxycombustion, petrochemicals, power plants, the chemical industry, and steel manufacturing, it is possible to enhance energy efficiency and reduce harmful emissions such as nitrogen oxides while enabling cost-efficient CO_2 capture. The versatility of OTM technology further extends to life science research and medical fields, for instance, providing an optimal environment for cellular growth and viability in cell culture systems and ensuring a reliable and efficient supply of oxygen for medical treatments.

The OTM can be employed in a hybrid form of 4-end and 3-end reactors in high-temperature industrial processes.[6,7] The 4-end reactor directly integrates with oxy-fuel power plants, allowing direct contact with the heat-gas stream. The recirculated combustion gas serves as a sweep gas on the permeation side of the membrane, thus providing oxygen for combustion. The fuel gas predominantly contains CO_2 and dual-phase membranes primarily composed of perovskite and fluorite crystal structures are widely used because of their chemical stability under harsh conditions. However, they suffer from low oxygen permeability, insufficient for supplying oxygen for combustion. Therefore, research on 3-end reactors is imperative for achieving an oxygen permeation flux of more than 10 mL cm^{-2} min^{-1}, which is crucial for commercializing OTMs in industry. Additionally, perovskite oxide materials have drawn significant attention as 3-end reactors due to their high permeability characteristics. In the 3-end reactor configuration, high-purity oxygen can be combined with recirculated combustion gas to enhance combustion efficiency, minimizing the release of toxic gases such as nitrogen oxides. In this case, the membrane permeate surface does not directly contact the combustion gas but uses a vacuum pump to collect the separated oxygen gas.

H. Bae, Y. Namgung, S.-J. Song
School of Material Science and Engineering
Chonnam National University
77 Yongbong-ro, Buk-gu, Gwangju 61186, Republic of Korea
E-mail: song@chonnam.ac.kr

G. D. Nam, J. H. Joo
School of Earth Science and Environmental Engineering
Gwangju Institute of Science and Technology
Gwangju 61006, Republic of Korea
E-mail: jhjoo@gist.ac.kr

K. Park, J.-Y. Park
Department of Nanotechnology and Advanced Materials Engineering
Sejong University
Seoul 05006, Republic of Korea

J. M. Serra
Instituto de Tecnología Química
Universitat Politècnica de València (UPV)-Consejo Superior de Investigaciones Científicas (CSIC)
46022 Valencia, Spain

The ORCID identification number(s) for the author(s) of this article can be found under https://doi.org/10.1002/sstr.202400095.

DOI: 10.1002/sstr.202400095

Various studies have been conducted to enhance the oxygen permeability of 3-end reactors, and the key factors governing the oxygen permeation are gas-exchange kinetics and oxygen-ion conductivity.[8] The oxygen-ion conductivity of perovskite oxides is strongly correlated with structural parameters such as the tolerance factor, octahedral factor, and lattice-free volume. By controlling these parameters, distortion can occur in the crystal lattice, resulting in changes in symmetry, vacancy concentration, and ion mobility, ultimately leading to high ion conductivity. In light of these perspectives, many studies have developed materials with high oxygen-permeation characteristics for application in 3-end reactors, based on the reported high oxygen permeation properties of the $BaCoO_3$ material group.[5,9,10] At the A-site, Ba ions with a $+2$ charge provide a sufficient concentration of oxygen vacancies, facilitating oxygen ion conduction. At the B-site, Co ions exhibit excellent catalytic properties and high electronic conductivity owing to the orbital overlapping of Co–O. Additionally, the low binding energy of Co–O favors oxygen ion migration. Furthermore, efforts are being made to overcome the phase transition and low oxygen-ion conductivity caused by the hexagonal crystal structure in undoped $BaCoO_3$ by incorporating carefully selected phase stabilizing cations in appropriate quantities at sites A and B.[11–13] In particular, it has been reported that incorporating La and Nb cations as phase stabilizes the cubic crystal structure over a wide temperature range and enhances oxygen-permeation characteristics.[9,14] These findings are further supported by several studies that have provided experimental and theoretical results for high oxygen-vacancy conduction and concentration in La or Nb-doped cases.[15–18] Recent efforts have been aimed at applying La- and Nb–co-doped materials in various energy conversion applications. Tang et al.[19] investigated the applicability of $Ba_{0.8}La_{0.2}Co_{0.88-x}Fe_xNb_{0.12}O_{3-\delta}$ as an oxygen transport membrane. Hu et al.[20] reported the excellent oxygen reduction reaction (ORR) activity and CO_2 tolerance of $Ba_{0.9}La_{0.1}Co_{0.7}Fe_{0.2}Nb_{0.1}O_{3-\delta}$ as a cathode material in intermediate-temperature solid oxide fuel cells (IT-SOFCs). They demonstrated its suitability as a cathode material with a high ORR activity and CO_2 tolerance. Zhou et al.[21] introduced $(Ba_{0.9}La_{0.1})_{0.95}Co_{0.7}Fe_{0.2}Nb_{0.1}O_{3-\delta}$ into symmetrical solid oxide fuel cells (SOFCs) and confirmed its high stability in both hydrogen and methane fuel conditions. In contrast, La and Nb have larger binding energies with oxygen, with values of 799 ± 4 and 771.5 ± 25.1 kJ mol^{-1}, respectively, compared to Ba and Co (561.9 ± 13.4 and 384.5 ± 13.4 kJ mol^{-1}, respectively).[22] Moreover, they possess positive effective charges within the crystal lattice that act as donors. This can suppress oxygen ion migration.

Motivated by prior findings, in this study, the stoichiometrically tailored lattice composition of $Ba_{0.95}La_{0.05}Co_{0.8}Fe_{0.12}Nb_{0.08}O_{3-\delta}$ (BLCFN) was optimized for oxygen transport membranes. The minimum amount of 0.05 mol La and 0.08 mol Nb were chosen based on previous studies.[9,17,23,24] Additionally, Fe was added to enhance the catalytic activity for the oxygen evolution reaction (OER) and improve thermodynamic stability.[25] The BLCFN membrane was fabricated by the tape-casting method, and a BLCFN porous layer was deposited to enhance the surface reactions, which are as important as oxygen-ion conductivity. Finally, its suitability for application in 3-end reactors was established by confirming its exceptional oxygen permeation characteristics under air/He conditions. Herein, we report for the first time that BLCFN membranes enable an unprecedented oxygen permeation flux, surpassing all previously reported OTMs, including $Ba_{0.5}Sr_{0.5}Co_{0.8}Fe_{0.2}O_{3-\delta}$ (BSCF). Furthermore, a comprehensive analysis was carried out to quantitatively elucidate the origin of its remarkable oxygen permeation and explore its potential for other electrochemical applications.

Additionally, as mentioned above, considering its potential applications beyond 3-end reactors, primarily driven by the electrochemical potential gradient of oxygen ion ($\nabla\eta_{O^{2-}}$), various driving forces ($\nabla\eta_{O^{2-}}$, $\nabla\eta_{h^{\cdot}}$, ∇T) and consequent cross effects are present. Therefore, we introduce an Onsager matrix capable of describing these phenomena. The mass/charge transport properties of the BLCFN under permeation operating conditions, where the chemical potential and thermal gradient were simultaneously applied, were interpreted based on Onsager's linear transport theory, considering the interference effect between the electron–ion and energy masses. The thermodynamic equilibrium defect-sensitive properties, such as nonstoichiometry and electrical conductivity, were systematically measured as functions of temperature and oxygen partial pressure. The experimental findings regarding the oxygen stoichiometry and electrical conductivity were coherently elucidated through defect chemical analysis, offering a detailed quantitative understanding of the diverse thermodynamic equilibrium values. This research highlights that BLCFN surpasses BSCF in terms of oxygen permeation efficiency, which was previously recognized as the most capable, and suggests that the intrinsic characteristics of BLCFN could be beneficial in a broad spectrum of electrochemical applications.

2. Results and Discussion

2.1. Phase Analysis

The powder X-ray diffraction (XRD) results for BLCF, BCFN, and BLCFN are presented in Figure S1a, Supporting Information. A cubic crystal structure was determined to be maintained with $Co \leq 0.5$ mol for BLCF, $Co \leq 0.7$ mol for BCFN, and $Co \leq 0.8$ mol for BLCFN. A further increase in the Co content led to a cubic-to-hexagonal phase transition in all three systems. The lattice constants were extracted through the Rietveld refinement of the XRD data, and the lattice-free volume (V_f) was calculated and plotted in Figure S1b, Supporting Information. V_f also increased with the Co content, and the highest value is confirmed in the BLCFN. The total electrical conductivity and oxygen permeation flux improved with increasing Co content, with BLCFN demonstrating the highest performance in both aspects, as shown in Figure S1c,d, Supporting Information. The BLCFN membrane with a thickness of 0.7 mm exhibited a high oxygen permeation flux of 3.92 mL cm^{-2} min^{-1} at 950 °C, using air/He with a 500 mL min^{-1} flow rate. Therefore, $Ba_{0.95}La_{0.05}Co_{0.8}Fe_{0.12}Nb_{0.08}O_{3-\delta}$ (BLCFN) was finally selected. The XRD pattern of the BLCFN is presented in **Figure 1**a. The lattice cubic constant and theoretical density of the single-phase cubic structure of BLCFN were determined through Rietveld refinement, yielding values of 4.08 Å and 6.03 g cm^{-3}, respectively. From the in-situ high-temperature XRD pattern

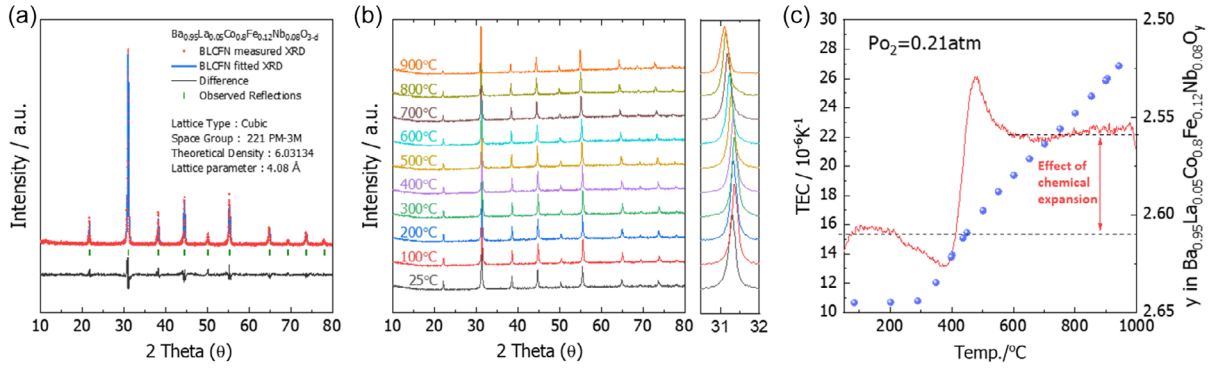

Figure 1. a) XRD pattern and profile matching result, b) in situ XRD pattern in the temperature range of 25–900 °C, and c) variation of TEC and oxygen content with temperature for BLCFN.

in Figure 1b, it can be ascertained that the cubic crystal structure is maintained in the temperature range from room temperature to 900 °C. The (110) diffraction peaks shift toward the lower angles around 400 °C. This is consistent with the thermal expansion behavior as a function of the temperature, as plotted in Figure 1c. The TEC exhibited values of between 14×10^{-6} and $16 \times 10^{-6}\,K^{-1}$ in the temperature range below 400 °C and increased significantly around 400 °C, reaching a value of $22 \times 10^{-6}\,K^{-1}$ in the temperature range of 600–1000 °C. This chemical expansion is attributed to the partial reduction of B-site cations and the associated oxygen-vacancy formation above 400 °C, leading to a higher averaged cation radius in the B-site sublattice. Indeed, a similar trend was observed in the oxygen stoichiometry with temperature.

2.2. Oxygen Permeability

In this study, to verify the oxygen permeability and elucidate the permeation mechanism of BLCFN, an oxygen transport membrane was fabricated using tape-casting techniques and examined in accordance with the thickness of the membrane. **Figure 2**a–c shows the microstructures of the BLCFN membrane coated with the BLCFN active layer. Applying the BLCFN active layer aims to enhance oxygen permeability by increasing the number of surface active sites for the gas-exchange reaction. The cross-sectional analysis reveals an active layer thickness of approximately 15 μm, exhibiting good porosity and adhesion at the interface with the membrane without any delamination. The membrane had a thickness of 84 μm. In this study, when the sweep gas was introduced at a flow rate of 500 mL min^{-1} on the permeate side, the N_2 concentration was detected to be less than 0.01%. These findings suggest that the pores observed in the SEM image can be considered closed pores and are negligible.

As mentioned earlier, the sweep gas was introduced at a flow rate of 500 mL min^{-1} on the feed and permeate sides. An insufficient supply of sweep gas on both sides led to a decline in the driving force for oxygen permeation. This reduction can be ascribed to the accumulation and depletion of O_2 at the membrane surface, resulting in a decrease in oxygen permeability. This phenomenon is commonly referred to as concentration polarization.[5,26] Thus, it is essential to eliminate the influence of concentration polarization on the oxygen permeation to achieve precise permeability values. As detailed in Figure S2, Supporting Information, the oxygen permeability exhibited a substantial enhancement as the gas flow rate increased at both ends of the membrane, reaching saturation at a gas flow rate of 500 mL min^{-1}. Thus, in this study, the impact of concentration polarization can be effectively minimized by adjusting the sweep gas flow rate to 500 mL min^{-1}.

To confirm the effect of the active coating layer on the permeability of the BLCFN membrane, the oxygen flux was assessed with and without the BLCFN coating layer, as illustrated in Figure 2d. Without the active layer, the oxygen permeation flux of the bare membrane was 10.1 mL cm^{-2} min^{-1} at 900 °C under air/He, and the activation energy was 0.44 eV. Conversely, the membrane with BLCFN active layer showed an improved oxygen flux of 12.4 mL cm^{-2} min^{-1} at 900 °C. Additionally, the activation energy of oxygen permeability was 0.25 eV, and this decreased activation energy is reported to be associated with the amelioration of surface reaction. These findings show that the application of BLCFN as an active layer can lower the activation energy for oxygen permeation, which can contribute to the improvement of the oxygen flux.

To examine the influence of the coating layers on each side of the membrane and their respective contributions to permeability improvement, the oxygen permeation flux was assessed by selectively adopting the BLCFN active layer solely on either the feed or permeate sides, as shown in Figure 2d. The membrane coated on the permeate side displayed a 32% improvement in oxygen flux (11.09 mL cm^{-2} min^{-1}) at 850 °C compared with the bare membrane (8.39 mL cm^{-2} min^{-1}), while the membrane coated on the feed side showed only a marginal increase (8.65 mL cm^{-2} min^{-1}). This indicates that the surface reaction of oxygen excorporation on the permeate side acts as the primary rate-limiting step (RLS), rather than oxygen incorporation on the feed side.

The oxygen permeability of the oxygen transport membrane is determined not only by operating conditions such as temperature, flow rate, and P_{O_2} differences across the membrane, but also by structural properties such as membrane type, and membrane thickness. To reduce the thickness of the membrane to less than 100 μm, it is typically necessary to fabricate a supported type of membrane. Due to the thick support, concentration polarization occurs, which commonly results in decreased oxygen

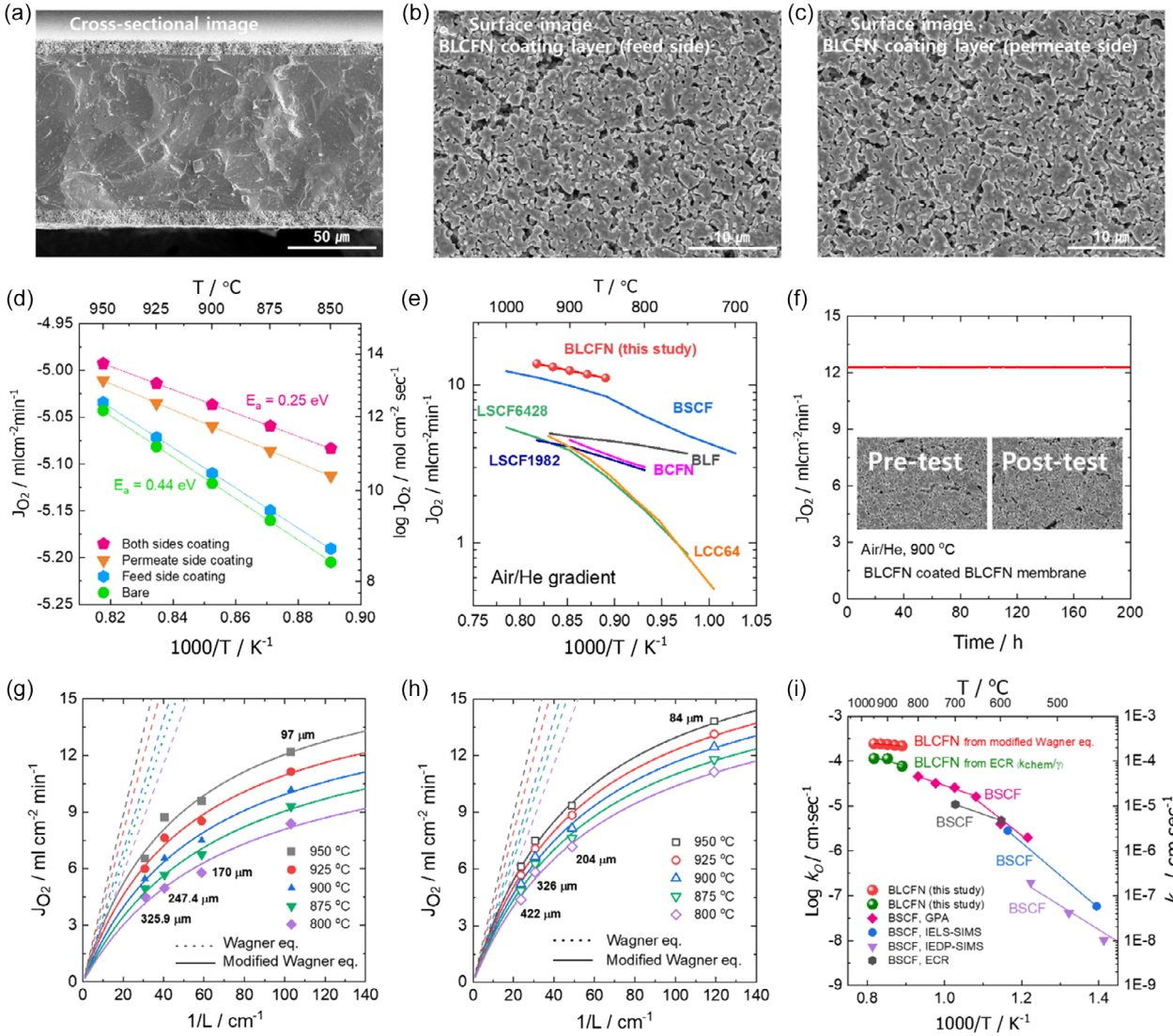

Figure 2. Microstructures of coated BLCFN membrane: a) cross-sectional image, b) feed side active layer (BLCFN), c) permeate side active layer (BLCFN). d) Oxygen permeation flux with and without BLCFN active layer. e) Comparison of oxygen permeability of BLCFN with previously reported single-phase membranes.[5,14,27–30] f) Oxygen permeation stability test of BLCFN membrane. Dependence of oxygen permeation fluxes on inverse thickness of BLCFN membrane g) without and h) with active layer. i) Surface exchange coefficient of BLCFN membrane compared with BSCF using GPA (isotope exchange with gas-phase analysis), IELS (isotope exchange line scanning technique), IEDP (isotope exchange depth profiling), and ECR (electron cyclotron resonance) methods.

permeability. Therefore, directly comparing the permeability of our free-standing membrane and supported membrane may be challenging. Despite these considerations, the permeability value of the free-standing membrane in this study is significant because it minimizes the effects of concentration polarization, thereby providing a system to evaluate the intrinsic permeability of the membrane material. While directly comparing the oxygen permeability of BLCFN with other reported membranes may be challenging due to differences in structural characteristics and operational conditions, it is helpful to understand the permeation behavior of materials because comparisons are made between membranes with similar ranges of thickness. To validate the remarkable oxygen permeability achieved by the BLCFN membrane in this study, Figure 2e presents a comparison of previously reported oxygen permeation fluxes for single-phase membranes[5,14,27–30] in accordance with the temperature within an air/inert gas (He or Ar) gradient. Additional details are presented in **Table 1**. The oxygen fluxes of a membrane within a comparable thickness range (20–84 μm) were shown for comparative analysis, as membrane thickness plays a significant role in determining oxygen permeability. The designed BLCFN exhibits the highest oxygen permeability among the oxygen transport membranes reported to date. For example, BSCF with a perovskite structure is regarded as a membrane material that exhibits exceptional oxygen permeability owing to its highest conductivity. However, at 900 °C, BLCFN membrane demonstrates

Table 1. Oxygen permeability of BLCFN-coated BLCFN membrane comparison with previously reported single-phase membranes.[5,14,27–30]

Membrane	BLCFN (monolithic)	BSCF (asymmetric)	BLF (asymmetric)	BCFN (asymmetric)	LCC64 (asymmetric)	LSCF1982 (asymmetric)	LSCF6428 (asymmetric)
Thickness [μm]	84	70	46	20	10	12	20
Flow rate [mL min^{-1}]	500/500	300/400	200/150	220/80	200/120	200/100	300/750
Catalytic layer	BLCFN	BSCF	BLF	BCFN	LCC64	LSCF1982	LSCF6428
J_{O_2} @ 900 °C [mL cm^{-2} min^{-1}]	12.4	9.9	4.7	4.5	4.1	3.8	4.1

approximately 25% higher oxygen permeability than the BSCF membrane. Therefore, BLCFN exhibits not only excellent phase stability over room-to-operating temperatures but also unprecedented oxygen permeability comparable to that of BSCF.

The stability of oxygen permeation under the operating conditions is a crucial aspect of the BLCFN membranes. The oxygen permeation stability of the BLCFN membrane at 900 °C under air/He condition is illustrated in Figure 2f. The inset SEM images show the pre-and post-test surface microstructures of the BLCFN active layers. The BLCFN-coated BLCFN membrane demonstrated a highly stable oxygen permeation flux of 12.4 mL cm^{-2} min^{-1} at 900 °C for over 200 h. The oxygen permeation stability was further supported by SEM surface images, which revealed no change in the pre- and post-test surface microstructures of the BLCFN active layer. XRD analysis of the BLCFN-coated BLCFN membrane before and after the permeation test was also performed, and it was confirmed that the cubic perovskite phase was maintained without a secondary phase (Figure S3a, Supporting Information). Additionally, an evaluation of the CO_2 tolerance was conducted for the BLCFN membrane. Helium gas, mixed with 1%, 3%, and 5% CO_2, was injected as the sweep gas, while air was used as the feed gas, and the results are shown in Figure S3b, Supporting Information. As the amount of CO_2 increases, the decrease in oxygen permeability becomes greater due to more CO_2 adsorption at the surface. However, it can be observed that the oxygen permeability values recover when transitioning from an environment with CO_2 to one without it. Therefore, despite the reduction in oxygen permeability in environments with CO_2, the fact that permeability recovers in the absence of CO_2 suggests that CO_2 does not degrade the composition of the membrane.

In accordance with our earlier publication, the oxygen permeation flux within the range of membrane thicknesses investigated in this study can be described by a modified Wagner equation, as follows.[31–33]

$$J_{O_2} \approx -\frac{1}{1+(2L_c/L)}\frac{C}{L} = \frac{C}{L+2L_c} \quad (1)$$

where C is a constant denoting the specific oxygen flux at a given temperature under air/He gradient conditions, and L_c, calculated as the diffusion coefficient (D_O) ratio to the surface exchange coefficient (k_o), represents the characteristic thickness. This value indicates the point at which the oxygen flux is predominantly governed by surface exchange rather than bulk diffusion. The unknown parameters C and L_c can be determined through nonlinear least-squares fitting, considering these two variables. For the BLCFN membrane coated with the active layer, C and L_c were calculated as 2.3×10^{-7} mol cm^{-1} s^{-1} and 82 μm, respectively. In this study, when oxygen permeability follows the behavior described by Wagner's equation, it should increase proportionally as the thickness decreases. However, given the value of L_c of 82 μm, surface exchange reactions cannot be ignored in this thickness range. Therefore, the relationship between the inverse thickness of the membrane and the oxygen flux shows a nonlinear behavior, indicating that it follows a modified Wagner equation, which accounts for surface exchange reactions.

Figure 2g,h show the oxygen flux of the BLCFN membrane with or without the active layer as a function of inverse thickness in the temperature range from 850 to 950 °C. According to Wagner's equation, when bulk diffusion is considered the rate-limiting step, there should be a linear correlation between the inverse thickness and oxygen flux. However, it is observed that the relationship between the inverse thickness-dependent oxygen flux deviates from linearity under the influence of surface modification.[34] Consequently, Wagner's equation is not appropriate for describing oxygen permeation behavior under these conditions. To address this, a modified Wagner equation was employed, and the solid line obtained from the fitting process closely aligned with the experimental data, indicating good agreement between the fitting results and actual measurements. The findings suggest that within the thickness range of 84–422 μm, the oxygen permeation mechanism of BLCFN is similarly determined by both bulk diffusion and surface exchange reaction.

To gain a more comprehensive understating of the interfacial reaction kinetics of OTMs, electrical conductivity relaxation (ECR) measurements, SIMS, and permeation model proposed by Zhu et al.[35,36] can be introduced. In this study. the interfacial reaction kinetics of BLCFN determined through oxygen permeation flux were compared with those determined through ECR measurements (Figure S4, Supporting Information), as shown in Figure 2i. For comparison, the temperature-dependent k_O values of BSCF derived via SIMS in previous studies[37,38] are also presented. Given that the k_O values in Figure 2i were obtained using distinct experimental methods and conditions, a direct comparison may not be unreasonable. However, it serves as a valuable tool for comprehending the significance and reliability of the k-value of BLCFN derived in this study.

$$D_O = \frac{RT\sigma_{ion}}{4F^2C_o} \quad (2)$$

where R, T, C_0, and F represent the gas constant, temperature, total concentration of lattice oxygen, and Faraday constant, respectively. Thus, by incorporating the values of L_c and D_O, the nominal surface exchange coefficient can be determined.

In this study, the calculated k_O values for the coated BLCFN membrane represent the average values obtained from both sides of the membrane owing to its exposure to an oxygen partial pressure gradient in air/He. The chemical surface exchange coefficient (k_{chem}) obtained from ECR surpassed the self-surface exchange coefficient owing to the presence of an additional chemical potential in a non-equilibrium state. Consequently, k_O can be obtained by dividing k_{chem} by the thermodynamic factor as follows

$$k_O = \frac{1}{\gamma} \times k_{chem} \tag{3}$$

$$\gamma = \frac{1}{2RT} \times \frac{\partial(\mu_{O_2})}{\partial \ln C_O} = \frac{1}{2} \times \frac{\partial \ln P_{O_2}}{\partial \ln C_O} \tag{4}$$

The thermodynamic factor of the BLCFN can be calculated using TGA. The calculated k_O values ($k_O = 2.4 \times 10^{-4}\,cm\,s^{-1}$ at 950 °C) obtained from the modified Wagner equation exhibit a close similarity with the k_O values ($k_O = 1.1 \times 10^{-4}\,cm\,s^{-1}$ at 950 °C) from ECR. The comparison shown in Figure 2i also demonstrates a close similarity between the k_O value and the activation energy obtained from the oxygen flux and ECR in this study. These values are comparable to those reported for BSCF, which is well-known for its high permeation characteristics. This correspondence supports the reliability of the k_O values derived in this study.

2.3. Iso/Non-Isothermal Transport Properties

Based on irreversible thermodynamics, the motions of oxygen ions (denoted by *i*), holes (denoted by *h*), and heat energy (represented by *q*) in the BLCFN system can be described using a 2×3 Onsager matrix.[39]

$$\begin{pmatrix} J_i \\ J_h \end{pmatrix} = -\begin{pmatrix} L_{ii} & L_{ih} & L_{iq} \\ L_{hi} & L_{hh} & L_{hq} \end{pmatrix} \begin{pmatrix} \nabla\eta_i \\ \nabla\eta_h \\ \nabla T \end{pmatrix} \tag{5}$$

The coefficients L_{km} ($k, m = i, h$) and L_{qk} ($k = i, h$) represent the Onsager coefficients for isothermal and non-isothermal conditions, respectively. This implies that the flow of the *k*-type carrier can be influenced by both its own direct effects and the cross effect. The cross-effects can be further categorized as follows: 1) Under isothermal conditions ($\Delta T = 0$), interference between the flows of charged particles (ions and holes) is defined as the charge of transport (α_k^*); and 2) Under non-isothermal conditions ($\Delta T \neq 0$), an interference between the flow of mass and heat energy is defined as the reduced heat of transport (q_k^*).[40,41]

$$\alpha_i^* \equiv \left(\frac{J_h}{J_i}\right)_{\nabla\eta_e=0} = \frac{L_{hi}}{L_{ii}} \tag{6}$$

$$\alpha_h^* \equiv \left(\frac{J_i}{J_h}\right)_{\nabla\eta_i=0} = \frac{L_{ih}}{L_{hh}} \tag{7}$$

$$L_{kq(k=i,h)} = \sum_{m=i,\,h} L_{km}\left(\overline{S}_m + \frac{q_m^*}{T}\right) \tag{8}$$

The physical meaning of α_i^* (or α_h^*) is the number of holes (ions) carried by a single mobile oxygen ion (hole) when no electrochemical potential exists for the holes (ions). The physical meaning of q_k^* is the amount of heat energy carried by the mass flow without a temperature gradient, which represents the exchange of heat energy with the surroundings to maintain isothermal conditions. In this case, the partial molar enthalpy of component $\overline{H}_m$ was excluded.

The correlation between L_{km} and L_{qk} is mediated by the term $\overline{S}_m + q_m^*/T$ as shown in Equation (8). This represents the transported entropy $\overline{\overline{S}}_k (= \overline{S}_m + q_m^*/T)$, which is expressed in terms of the ionic and electronic thermoelectric power θ_k^{st} in the Soret equilibrium.[40,42,43]

$$\theta_k^{st} = \frac{1}{z_k F}\left(\frac{d\eta_k}{dT}\right)_{J_O=0} = -\frac{1}{z_k F}\overline{\overline{S}}_k \tag{9}$$

The 2×2 isothermal transport coefficient matrix L_{km} was obtained from the current–voltage characteristics of the ion-blocking polarization cell. A schematic of the asymmetric electrochemical cell is shown in **Figure 3**a. A constant current was applied between terminals e and f of the electrochemical cell, and real-time electrical signals *U* and *V* were observed between the ion probes (a, b) and the electron probes (c, d). These signals can be described as functions of the electrochemical potentials of oxygen ions and holes.

$$-2FU = \Delta\eta_i \approx \ell\nabla\eta_i \tag{10}$$

$$FV = \Delta\eta_e \approx \ell\nabla\eta_e \tag{11}$$

where *F* represents Faraday's constant and ℓ denotes the distance between the ion (or electron) probes. During the initial moment when a constant current is applied to the sample in the open-circuit condition, the voltage drop measured ($\Delta U = \Delta V$) is solely determined by the total electrical conductivity, as there is no occurrence of chemical diffusion of oxygen ions.

$$\sigma_{tot} = \frac{\ell}{A}\left(\frac{I}{\Delta V}\right) \tag{12}$$

where *A* represents the cross-sectional area of the specimen. When oxygen within the specimen no longer distributes uniformly ($\Delta\delta \neq 0$) and evolves out of the reversible electrode under the applied electrostatic field, a concentration imbalance occurs, leading to chemical polarization. The chemically induced transport of oxygen ions occurs in a direction opposite to that driven by an electric field. Consequently, a steady state is achieved, where these counteractive fluxes offset each other, resulting in complete quiescence of oxygen-ion migration across the entire specimen. Electronic conductivity (σ_e') and ionic charge of transport (α_i^*) can be expressed as below. Details of Equation (13) and (14) can be found elsewhere.[44]

$$\alpha_i^* = -\left(\frac{\nabla\eta_i}{\nabla\eta_e}\right)_{J_i=0} = \frac{2U}{V} \tag{13}$$

$$\sigma'_e = \frac{\ell}{A}\left(\frac{I}{V}\right)_{J_i=0} \tag{14}$$

As observed in the experiment, the typical polarization/depolarization behavior is illustrated in Figure S5a, Supporting

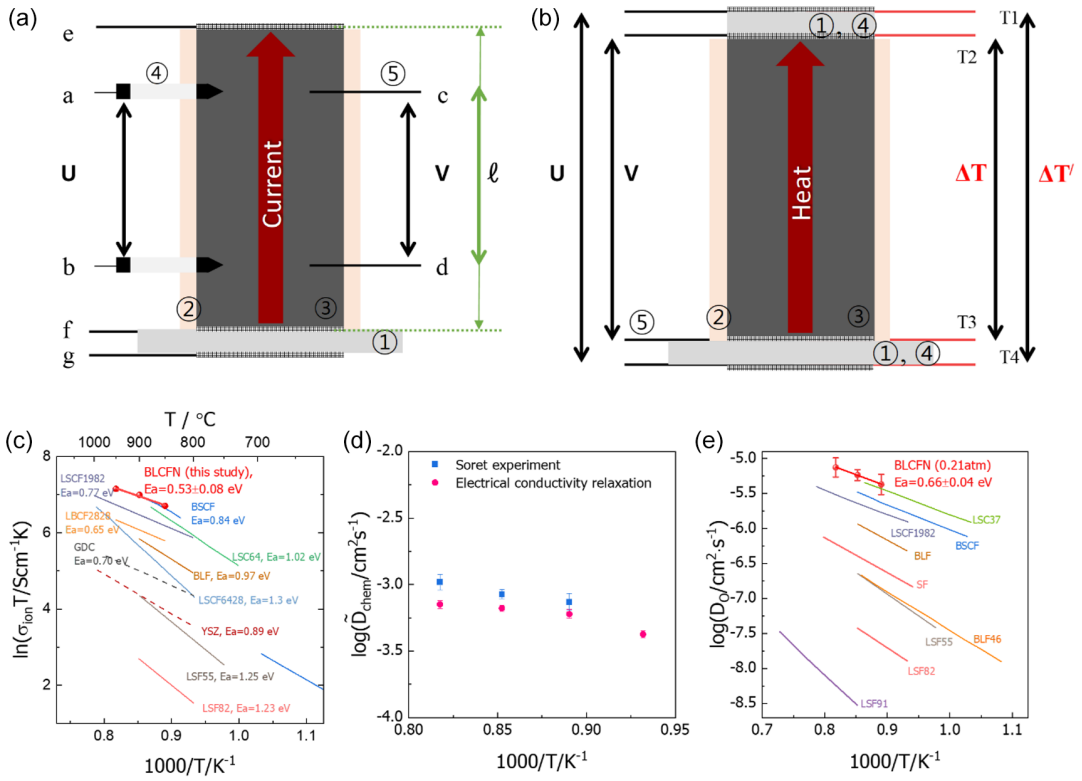

Figure 3. Schematics of a) isothermal and b) non-isothermal polarization cells. ① YSZ electrolyte, ② ceramabind #643, ③ $Ba_{0.95}La_{0.05}Co_{0.8}Fe_{0.12}Nb_{0.08}O_{3-\delta}$ (sintered specimen), ④ ionic probe (YSZ), ⑤ electronic probe (Pt wire). Probes are (a,b): inner ionic probe, c,d): inner electronic probe, e–g): reversible electrode. Temperature differences are represented as $\Delta T = T3 - T2$, $\Delta T = T4 - T1$. The black line indicates Pt and the red line indicates Pt–Rd (10 wt%). c) Ion conductivity (σ_{ion}), d) chemical diffusivity (D_{Chem}), and e) self-diffusivity (D_O) of oxygen as a function of inverse temperature. The results for BLCFN are compared with the values of LSCF(LBCF),[47,70] BSCF,[37,48,71] LSC,[1,72] BLF,[15,49] LSF(SF),[50–53] YSZ,[45] and GDC.[46]

Information. Upon applying a constant current to the specimen in its equilibrium state, U and V exhibited an instantaneous and simultaneous sharp rise, characterized by an equal magnitude of increment. Thereafter, the value of U continued to decrease continuously with time, whereas V exhibited a continuous and gradual increase owing to the total current through the mixed conductor, given by $I = -2FJ_i + FJ_e$. Additionally, it should be noted that in the steady state, U is expected to ideally converge to zero. However, U approximated a certain nonzero value. This is indisputable experimental evidence demonstrating the interference effect (cross effect, $L_{ei} = L_{ie} \neq 0$) between oxygen-ions and electronic transport in BLCFN. Upon removing the applied constant current, both U and V exhibited an initial rapid decrease, and the depolarization curve gradually approached zero because of the chemical diffusion of oxygen.

Table 2 summarizes the values of σ_{tot}, σ_{el}, and α_i^* calculated from Equation (12)–(14). Additionally, the L_{km} matrix was constructed from the relationship with these quantities, as shown in Equation (15)–(17).[44]

$$L_{ii} = \frac{\sigma - \sigma'_e}{F^2(\alpha_i^* - 2)^2} \tag{15}$$

$$L_{ih} = \frac{\alpha_i^*(\sigma - \sigma'_e)}{F^2(\alpha_i^* - 2)^2} \tag{16}$$

$$L_{hh} = \frac{\alpha_i^*(\sigma - 4\sigma'_e) + 4\sigma'_e}{F^2(\alpha_i^* - 2)^2} \tag{17}$$

The oxygen-ion conductivity of the BLCFN (Figure 3c) was determined to be $1.04\ S\ cm^{-1}$ at 950 °C and 0.21 atm. Compared to other mixed ionic-electronic conducting (MIEC) oxides and solid electrolytes, BLCFN exhibits outstanding oxygen-ion conductivity and low activation energy. This result confirms the exceptional permeation characteristics of the BLCFN membrane. Arrhenius equation can describe the temperature dependence of oxygen-ion conductivity in the following form

$$\sigma_{ion} = \frac{1.9 \times 10^5}{T} \exp\left(-\frac{0.53\text{eV}}{kT}\right) \tag{18}$$

The total electrical conductivity, σ_{tot}, was measured as a function of temperature and oxygen partial pressure using the DC 4-probe method. The obtained σ_{tot} values are plotted in Figure S5b, Supporting Information, along with those obtained from the polarization cell. The consistency between the results of the two independent measurement methods indicated that the isothermal polarization experiments were conducted under well-controlled thermodynamic conditions, ensuring the reliability of the measurements.

Table 2. Extracted quantities from iso/non-isothermal polarization experiments.

Temperature [°C]	α_i^*	σ_{total} [S cm^{-1}]	σ_{el} [S cm^{-1}]	σ_{ion} [S cm^{-1}]	t_{ion}	$\bar{\bar{S}}_h$ [J mol−1 K−1]	D_T [cm^2 s^{-1}]
950	0.58	29.29	28.25	1.04	0.035	10.63	$(3.16 \pm 0.39) \times 10^{-3}$
900	0.54	27.63	26.70	0.93	0.033	9.86	$(2.97 \pm 0.41) \times 10^{-3}$
850	0.50	26.54	25.82	0.73	0.028	9.65	$(2.84 \pm 0.62) \times 10^{-3}$

The 2×1 non-isothermal transport coefficient matrix L_{kq} was obtained from thermopower measurements under Soret equilibrium conditions and a 2×2 matrix of L_{km}. The real-time values of U and V generated by the heat flow from the bottom to the top of the symmetrical polarization cell in Figure 3b were measured using in situ ion and electron probes. The electrochemical potentials of oxygen-ions and electron holes can be determined by correcting for the thermopower of YSZ (θ^{YSZ}) and Pt (θ^{Pt}) in U and V.

$$U = -\frac{\Delta(\eta_i - \mu_O^{ref})}{2F} - \int_{T_4}^{T_1} \theta^{Pt} dT + \theta^{YSZ}(\Delta T' - \Delta T) \tag{19}$$

$$V = \frac{\Delta \eta_h}{F} - \int_{T_3}^{T_2} \theta^{Pt} dT \tag{20}$$

The temporal variations of U, V, and ΔT under the temperature gradient are shown in Figure S5c, Supporting Information. V follows a monotonic relaxation curve; U initially decreases and then exhibits a slight increase over time, or vice versa, showing a similar pattern during the depolarization step. Furthermore, in Figure S5d, Supporting Information, the behavior of $\Delta\eta_h/F$ with respect to ΔT shows the hysteresis phenomenon. This is because of the time-dependent nature of the driving forces for the thermomigration of the oxygen component under Soret conditions. Initially, thermomigration is solely determined by ∇T. However, over time, $\nabla\delta$ becomes dominant, with chemical diffusion of mobile component O ($=O^{2-} + 2h^+$) kinetically governing the process.[45,46]

By employing a modified analytical solution for thermomigration kinetics, which describes the redistribution of mobile species under temperature gradients in a closed system, D_{chem} was extracted from the temporal behavior of $\Delta\eta_h$/F in Figure S5d, Supporting Information. A detailed derivation of the original analytical solution can be found elsewhere,[37] and we made appropriate modifications to accommodate our experimental conditions. The results are presented in Figure 3d along with the D_{chem} values obtained from ECR. The extracted D_{chem} values from the non-isothermal polarization experiment were slightly higher than those obtained from the ECR; however, they were within the same order of magnitude, and the temperature dependence was reasonably consistent. Considering the limitations of the conventional conductivity relaxation method, including the difficulty in precisely controlling the gas flow during the stepwise variation of pO_2 and the perturbation effects of surface exchange reactions, the results of the non-isothermal polarization experiment were deemed reliable. The other extracted quantities, transported entropy $\bar{\bar{S}}_h$ and thermal diffusivity D_T, are summarized in Table 2.

The oxygen self-diffusion coefficient, D_O is related to D_{chem} using Equation (21).

$$D_{Chem} = D_O f(\theta); \quad f(\theta) = \frac{1}{2}\left(\frac{\partial \ln P_{O_2}}{\partial \ln(3-\delta)}\right)_T \tag{21}$$

The thermodynamic enhancement factor $f(\theta)$ was calculated through TGA. The D_O of the BLCFN in the Arrhenius plot is shown in Figure 3d. It can be observed that the oxygen self-diffusivity of BLCFN exhibits higher values compared to well-known mixed conducting perovskite materials commonly used in membrane studies.[15,47–54]

Ionic and electronic thermoelectric power θ_k^{st} were calculated from the electrochemical potentials of ions/electrons at various ΔT using Equation (10), (19), and (20). The electronic thermopower $\theta_h{}^{st}$ was determined from the slope of $\Delta\eta_h/F$ with respect to ΔT obtained from V. Similarly, $\theta_i{}^{st} - S_O{}^{ref}/2F$ was obtained from the slope of $\Delta(\eta_i - \mu_O{}^{ref})/2F$ with respect to ΔT obtained from U. $\theta_i{}^{st}$ was then determined by correcting the term $S_O{}^{ref}/2F$.[55] The results are shown in Figure S5e,f, Supporting Information. The negative sign of $\theta_h{}^{st}$ indicates the p-type characteristic according to Wagner's definition,[42] suggesting that electronic conduction in BLCFN is predominantly governed by positively charged holes. Conversely, the positive sign of $\theta_i{}^{st}$ indicates the presence of negatively charged ionic charge carriers. Considering that only oxygen ions are mobile, negatively charged oxygen interstitials, rather than positively charged oxygen vacancies, may be the predominant ionic charge carriers in the BLCFN.

$$\begin{pmatrix} J_i \\ J_h \end{pmatrix} = -\begin{pmatrix} 5.6 \times 10^{-11} & 3.2 \times 10^{-11} & 6.4 \times 10^{-9} \\ 3.2 \times 10^{-11} & 3.4 \times 10^{-9} & 3.8 \times 10^{-8} \end{pmatrix} \times \begin{pmatrix} \nabla\eta_i \\ \nabla\eta_h \\ \nabla T \end{pmatrix}_{900\,°C,\ 0.21\,atm} \tag{22}$$

$$\begin{pmatrix} J_i \\ J_h \end{pmatrix} = -\begin{pmatrix} 4.7 \times 10^{-11} & 2.5 \times 10^{-11} & 5.3 \times 10^{-9} \\ 2.5 \times 10^{-11} & 3.2 \times 10^{-9} & 3.2 \times 10^{-8} \end{pmatrix} \times \begin{pmatrix} \nabla\eta_i \\ \nabla\eta_h \\ \nabla T \end{pmatrix}_{850\,°C,\ 0.21\,atm} \tag{23}$$

$$\begin{pmatrix} J_i \\ J_h \end{pmatrix} = -\begin{pmatrix} 3.5 \times 10^{-11} & 1.8 \times 10^{-11} & 3.5 \times 10^{-9} \\ 1.8 \times 10^{-11} & 2.5 \times 10^{-9} & 3.1 \times 10^{-8} \end{pmatrix} \times \begin{pmatrix} \nabla\eta_i \\ \nabla\eta_h \\ \nabla T \end{pmatrix}_{800\,°C,\ 0.21\,atm} \tag{24}$$

From Equation (8) and (9), L_{kq} was determined, and ultimately, a 2×3 Onsager matrix for the BLCFN was successfully completed, as shown in Equation (22)–(24). Both the cross-effect between the ion and electron flows and the cross-effect between mass and heat flows exhibit nonzero values. Moreover, the non-isothermal conditions revealed a higher coupling effect, as confirmed by the Onsager transport coefficients. Unlike in the 3-end reactor (Air/He), where $\nabla\eta_i$ primarily acts as the dominant driving force, these cross-effects are anticipated to be significant under the operating conditions where the influence of $\nabla\eta_h$ and ∇T cannot be neglected, such as air/methane reforming. Therefore, cross effects cannot be overlooked in such cases, and our 2×3 Onsager matrix is expected to serve as valuable background data applicable to these specific conditions.

2.4. Oxygen Nonstoichiometry and Electrical Conductivity

The $\delta - pO_2 - T$ plot of in **Figure 4**a shows a systematic trend of oxygen deficiency and a negative temperature derivative ($\partial\delta/\partial T < 0$) under the given thermodynamic conditions. This observation confirms the exothermic nature of the oxidation reaction. Additionally, a monotonic decrease in oxygen nonstoichiometry was observed as the oxygen partial pressure decreased. The relative partial molar quantities of oxygen mixing, $\Delta\overline{H}_O^M$ and $\Delta\overline{S}_O^M$, are associated with the non-ideality of the solid solution. $\Delta\overline{H}_O^M$ and $\Delta\overline{S}_O^M$ are defined by Equation (25)–(27) as follows

$$\Delta\overline{G}_O^M = \Delta\overline{H}_O^M - T\Delta\overline{S}_O^M = \mu_O - \frac{1}{2}\mu^o_{O_2}(g) = \frac{1}{2}RT\ln a_{O_2} \tag{25}$$

$$\Delta\overline{H}_O^M = h_O(\delta) - h_O^o = \left.\frac{\partial(\Delta\overline{G}_O^M/T)}{\partial(1/T)}\right|_\delta = \frac{R}{2}\left.\frac{\partial \ln P_{O_2}}{\partial(1/T)}\right|_\delta \tag{26}$$

$$\Delta\overline{S}_O^M = s_O(\delta) - s_O^o = \left.\frac{\partial\Delta\overline{G}_O^M}{\partial T}\right|_\delta = -\frac{R}{2}\left.\frac{\partial(T\ln P_{O_2})}{\partial T}\right|_\delta \tag{27}$$

In Figure 4b, it is observed that the value of $\Delta\overline{H}_O^M$ in the range of $\delta = 0.25$–0.40 increases from -122.66 ± 16.45 to -97.93 ± 7.38 kJ mol^{-1} as δ increases from 0.263 to 0.393, exhibiting a linear growth ($\partial\Delta\overline{H}_O^M/\partial\delta > 0$). This phenomenon occurs as the thermodynamic component O is incorporated, leading to less favorable mixing than the ideal solution, increasing in energy. This directly demonstrated the positive deviation of the BLCFN. The $\Delta\overline{S}_O^M$ is composed of the entropy change in the electronic state of 3 d orbitals of B-site transition metal ions and the configurational entropy $\Delta\overline{S}_{Conf}$ of the lattice oxygen ions. In the case of BLCFN, it was observed to increase slightly as the δ decreases. This behavior is consistent with statistical thermodynamic theory,[56–58] indicating that the behavior of $\Delta\overline{S}_O^M$ with respect to the δ is mainly governed by the dominant contribution of $\Delta\overline{S}_{Conf}$. $\Delta\overline{H}_O^M$ in Equation (26) is expressed further as follows, considering the structure elements within the system, satisfying the conservation of mass, site, and charge.

$$\begin{aligned}\Delta\overline{H}_O^M &= \left.\frac{\partial(\Delta\overline{G}_O^M/T)}{\partial(1/T)}\right|_\delta \\ &= \Delta H^o_{OX} + R\left(\sum\nolimits_{SEi}\nu_i\frac{\partial\ln\gamma_i}{\partial(1/T)} + 2\frac{\partial\ln\gamma_h}{\partial(1/T)}\right)_\delta\end{aligned} \tag{28}$$

The SEi denotes the specific combination of structure elements representing oxygen ions, while ν_i signifies the coefficients necessary to maintain charge neutrality, for example, $O^{2-} = O_O^X - V_O^{\cdot\cdot}$. Examining Equation (28), it becomes evident that the term combined with the gas constant R, referred to as excess enthalpy $\overline{H}_O^{M,XS}$, is a crucial factor directly influencing the non-ideal behavior because ΔH^o_{OX} is a temperature-dependent quantity. Accordingly, the positive deviation of BLCFN can be qualitatively explained by deviations in the activity coefficients ($\gamma_k \neq$ to 1) of ionic or electronic defects. Mizusaki et al.[59–62] interpreted this phenomenon as originating from ionic defects, as most MIEC perovskite oxides show a linear relation of $\Delta\overline{H}_O^M$ with respect to δ. They hypothesized that the activity coefficients of oxygen ion defects would exhibit a linear relationship with δ, deviating from a value of 1 by an α-factor. Given that $\Delta\overline{H}_O^M$ of BLCFN exhibits linearity with δ, we have applied this logic to design non-ideal defect structures.

For defect chemical analysis, defining the lattice molecular formula and the majority defect species is essential. Based on the thermopower measurement results, oxygen interstitial defects are expected to prevail in BLCFN. Additionally, it has been reported that a similar structured compound, $BaCo_{0.7}Fe_{0.22}Nb_{0.08}O_{3-\delta}$,[16] shows an increasing trend of σ_{ion} with increasing aO_2, an unquestionable characteristic of ion conduction attributed to oxygen interstitials. Although it is not possible to completely exclude the possibility of oxygen vacancies, oxygen interstitials are considered the majority of ionic defects. Therefore, the lattice molecular formula of BLCFN is defined as $ABO_{2.5+\delta}$ or $ABO_{2+\delta}$, enabling the interpretation of the migration of excess oxygen through vacant oxygen lattice sites. This interpretation preserves the well-known crystallographic concept of perovskite oxides. In contrast, according to the report on $BaCo_{1-x-y}Fe_xNb_yO_{3-\delta}$ and $Ba_{1-x}Sr_xCo_{1-y}Fe_yO_{3-\delta}$ systems,[10,16] it has been observed that Co ions exist in both +2 and +3 oxidation states, while most Fe ions are in the +3 oxidation state. Thus, by defining the stoichiometric composition as ABO_2, it becomes possible to consider the electronic defect of $B_B^{\cdot}$ (B^{3+}) with an effective charge of +1. Consequently, the charge neutrality condition of the BLCFN can be expressed as follows

$$2[O''_i] = 3[Nb_B^{\cdot\cdot\cdot}] + [La_{Ba}^{\cdot}] + \sum[B_B^{\cdot}] \tag{29}$$

where [] represents the defect concentration, and the oxygen nonstoichiometry can be defined based on the equation presented earlier.

$$\delta = [O''_i] - \frac{1}{2}[La_{Ba}^{\cdot}] - \frac{3}{2}[Nb_B^{\cdot\cdot\cdot}] = \frac{1}{2}([Co_B^{\cdot}] + [Fe_B^{\cdot}]) \tag{30}$$

Site conservation follows the following equations

$$[O''_i] + [V_i^{\times}] = 1 \tag{31}$$

$$[Fe_B^{\cdot}] + [Fe_B^{\times}] = 0.12 \tag{32}$$

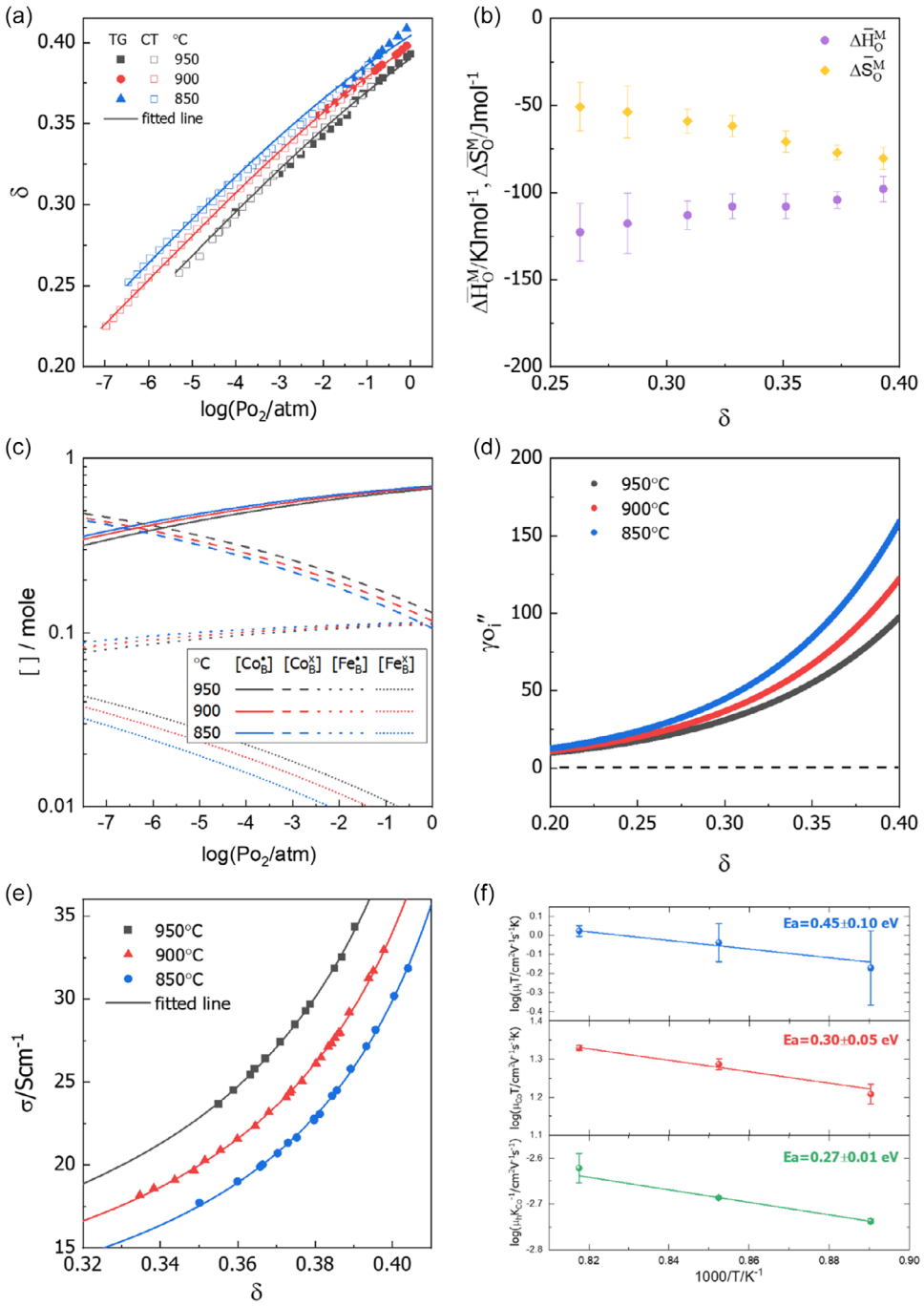

Figure 4. a) δ–pO_2–T plot of BLCFN, b) partial molar quantities of oxygen mixing, c) defect concentration as a function of T and pO2, d) activity coefficients of interstitial oxygen as a function of T and pO_2, and e) total conductivity of BLCFN as a function of T and δ, f) mobilities versus 1/T.

$$[Co_B^{\bullet}] + [Co_B^{\times}] = 0.8 \tag{33}$$

$$[Nb_B^{\bullet\bullet\bullet}] = 0.08 \tag{34}$$

$$[La_{Ba}^{\bullet}] = 0.05 \tag{35}$$

The charge disproportionation reaction and its equilibrium constant can be expressed by the following equations

$$Co_B^{\bullet} + Fe_B^{\times} \leftrightarrow Co_B^{\times} + Fe_B^{\bullet} \tag{36}$$

$$K_D = \frac{[Co_B^{\times}][Fe_B^{\bullet}]}{[Co_B^{\bullet}][Fe_B^{\times}]} \tag{37}$$

The external equilibrium reaction between solid and gas phase, along with its equilibrium constant, can be described as follows

$$\frac{1}{2}O_2 + V_i^{\times} + 2Co_B^{\times} \leftrightarrow O_i'' + 2Co_B^{\bullet} \tag{38}$$

$$K_{OX} = \frac{\gamma_{O_i''}[O_i'']{[Co_B^{\bullet}]}^2}{a_{O_2}^{1/2}[V_i^{\times}]{[Co_B^{\times}]}^2} \tag{39}$$

The activity coefficient of the oxygen interstitial $\gamma_{O_i''}$ is defined as a function of δ using the α-factor proposed by Mizusaki.[60]

$$\ln \gamma_{O_i''} = \alpha \cdot \delta \tag{40}$$

The relationship between δ and aO_2 can be derived using Equation (29)–(39) as follows

$$\log a_{O_2} = -2\log K_{OX} + 2\log\frac{[O_i']}{[V_i^{\times}]} + 4\log\frac{[Co_B^{\bullet}]}{[Co_B^{\times}]} + \frac{2}{2.303}\alpha\delta \tag{41}$$

$$[Co_B^{\bullet}] = \frac{-[(0.12-2\delta)K_D + 0.8 + 2\delta] + \sqrt{[(0.12-2\delta)K_D + 0.8 + 2\delta]^2 + 6.4(K_D-1)\delta}}{2(K_D-1)} \tag{42}$$

The derived relationship was nonlinearly fitted to δ as a function of temperature and oxygen partial pressure, and the best-fitted results are shown as solid lines in Figure 4a. The extracted quantities, K_{OX}, K_D, and the deviation factor α, showed the following temperature dependence

$$K_{ox} = (3.07 \pm 0.16) \times 10^{-2} \exp\left(\frac{1.61 \pm 0.01\text{eV}}{kT}\right) \tag{43}$$

$$K_D = (2.23 \pm 0.13) \times 10^{-1} \exp\left(\frac{0.26 \pm 0.01\text{eV}}{kT}\right) \tag{44}$$

$$\alpha = (16.78 \pm 0.10) \times 10^3 T^{-1} - (2.27 \pm 0.08) \tag{45}$$

The defect concentrations were calculated from K_{OX} and K_D and are shown in Figure 4c as functions of temperature and oxygen partial pressure. It can be observed that $[Co_B^{\cdot}]$ dominates, and as the temperature increases at a fixed oxygen partial pressure, $[Co_B^{\cdot}]$ decreases while $[Co_B^{X}]$ increases. In the isotherm, as the oxygen partial pressure increases, both $[Co_B^{\cdot}]$ and $[Fe_B^{\cdot}]$ increase, showing a slightly higher increment for $[Co_B^{\cdot}]$, suggesting that Co ions may have a greater influence on the electrical conductivity compared to Fe ions.

The positive sign of the deviation factor α has been confirmed, providing a quantitative explanation for the positive deviation phenomenon observed in BLCFN. Figure 4d shows the $\gamma_{O_i''}$ values as a function of δ, calculated using Equation (40). BLCFN consistently exhibits $\gamma_{O_i''} > 1$ under all measured thermodynamic conditions, and as the temperature increases and δ decreases, the system approaches the ideal solution.

The total electrical conductivity σ_{tot} is the sum of the ionic conductivity σ_{ion} and the electronic conductivity σ_{el}. Further, σ_{el} consists of two contributions: small polaron hopping conduction of localized holes (σ_{el_loc}) and band conduction of free holes (σ_{el_del}). Each conductivity can be defined as the product of defect concentration and mobility.

$$\sigma_{tot} = \sigma_{ion} + \sigma_{el\_loc} + \sigma_{el\_del} \tag{46}$$

$$\sigma_{ion} = \sigma_i^0[O_i'][V_i] \tag{47}$$

$$\sigma_{el\_loc} = \sigma_{h,Co}^0[Co_B^{\bullet}][Co_B^{X}] + \sigma_{h,Fe}^0[Fe_B^{\bullet}][Fe_B^{X}] + \sigma_{h,CoFe}^0[Co_B^{\bullet}][Fe_B^{X}] \tag{48}$$

$$\sigma_{el\_del} = \sigma_h^0 p \tag{49}$$

$$\sigma_k^0 = |Z_i^{\text{eff}}|F\mu_k V_m^{-1} \tag{50}$$

σ_{el_loc} was considered the conduction through Co^{2+}/Co^{3+} sites, Fe^{2+}/Fe^{3+} sites, and conduction involving Co/Fe sites. σ_{el_del} was accounted for by considering the presence of free holes from the ionization reaction through the Co site, as shown in the following equation

$$Co_{Co}^{\times} + h^{\bullet} \leftrightarrow Co_{Co}^{\bullet};\quad p = \frac{1}{K_{Co}}\frac{[Co_{Co}^{\bullet}]}{[Co_{Co}^{\times}]} \tag{51}$$

The consideration of σ_{el_del}, despite constructing defect structure with the localized electron, is reasonable because of the significantly higher mobility of free holes compared to localized holes in general. Because of their higher mobility, the conduction effect of free holes can be adequately represented in terms of conductivity, although their concentration may be lower than that of localized electron defects. The dominant contribution to the conduction characteristics of the BLCFN was attributed to polaron hopping through the Co site. The experimental evidence in Figure S1a, Supporting Information, demonstrates that increasing Co concentrations result in higher electrical conductivity in the BCFN. This trend is consistent with observations in the BSCF.[63] This is also confirmed in Figure 4c. Based on these findings, it is assumed that free holes can be generated primarily through Co sites rather than through Fe sites.[64,65]

The total conductivity, shown in Figure 4e, was fitted using the mobility in Equation (50) as a fitting parameter. The concentration of each defect species is expressed as a function of δ, as given by Equation (31–35, 39, and 42). The oxygen ion mobilities μ_i were fixed by calculating them from σ_{ion} obtained in an isothermal polarization experiment. For the hole mobility μ_h, μ_h/K_{Co} was used as a fitting parameter because it is difficult to directly obtain K_{Co} through defect chemical analysis. The fitting results showed that μ_{Fe} and μ_{CoFe} were close to zero, indicating negligible contribution to the conduction. Only μ_{Co} exhibited a significant value. This suggests that most of the hopping conduction occurs through the Co site. The mobility of the charge carriers exhibits the following temperature dependence

$$\mu_i = \frac{(7.4 \pm 2.9) \times 10}{T}\exp\left(-\frac{0.45 \pm 0.10\text{eV}}{kT}\right) \tag{52}$$

$$\mu_{Co} = \frac{(3.59 \pm 0.71) \times 10^2}{T}\exp\left(-\frac{0.30 \pm 0.05\text{eV}}{kT}\right) \tag{53}$$

$$\mu_h K_{Co}^{-1} = (3.02 \pm 0.01) \times 10^{-2} \exp\left(-\frac{0.27 \pm 0.01\text{eV}}{kT}\right) \quad (54)$$

In the case of μ_h/K_{Co}, the activation energy (0.27 eV) was assumed to correspond to the ionization equilibrium reaction because of the negligible temperature-dependent nature of the band conduction mechanism.

3. Conclusions

The $Ba_{0.95}La_{0.05}Co_{0.8}Fe_{0.12}Nb_{0.08}O_{3-\delta}$ (BLCFN) membrane demonstrated exceptional oxygen permeation flux (12.4 mL cm^{-2} min^{-1} at 900 °C, Air/He) and long-term stability. To the best of our knowledge, this represents a world-record performance, outperforming those previously reported for single-perovskite membranes under air/He conditions. These findings were quantitatively elucidated through electrochemical analysis of the mass and charge transport properties under irreversible conditions and through defect chemical analysis of the thermodynamic equilibrium properties. An iso/non-isothermal electrochemical polarization cell was implemented to measure the Onsager transport coefficient matrix, and the oxygen nonstoichiometry and total conductivity were systematically measured using thermodynamic variables (T, pO_2). The diffusion coefficient, ionic conductivity, and surface reaction constant were quantitatively extracted to provide scientific support for the oxygen permeation characteristics of the BLCFN. It has also been verified that the interference coefficients are significant and that the interference between the mass and heat energy is considerably larger than that between charge carriers. This highlights the significance of the temperature gradient as an essential factor, in addition to the electrochemical potential, for mass and charge transport in mixed conductors. Based on defect chemical analysis, the experimental results of oxygen stoichiometry and electrical conductivity have been consistently explained, providing quantitative insights into various thermodynamic equilibrium values. In summary, this study demonstrates that BLCFN exhibits a higher oxygen permeation performance than BSCF, which is known for exhibiting the previous highest capability, and suggests that the fundamental properties of the BLCFN material may be applicable to a variety of other electrochemical applications.

4. Experimental Section

Material Preparation and Characterization: Polycrystalline samples of $Ba_{0.95}La_{0.05}Co_xFe_{1-x}O_{3-\delta}$ (BLCF), $BaCo_xFe_{0.92-x}Nb_{0.08}O_{3-\delta}$ (BCFN), and $Ba_{0.95}La_{0.05}Co_xFe_{0.92-x}Nb_{0.08}O_{3-\delta}$ (BLCFN) were prepared using a conventional solid-state reaction method. The starting materials, $BaCO_3$, La_2O_3, Fe_2O_3, Co_2O_3, and Nb_2O_5, were meticulously weighed in the desired stoichiometric ratios and then mechanically mixed using zirconia balls in an isopropyl alcohol solvent to achieve uniform mixing. Subsequently, the mixed powders underwent a thorough drying process to eliminate any residual moisture before undergoing calcination at 1000 °C. After the calcination process, the powder was further pulverized using a mortar and pestle, and then sieved through a 25 μm metal mesh to obtain a fine powder with controlled particle size distribution. The powder was shaped into rectangles or disks according to the purpose of the experiment and subjected to cold isostatic pressing (CIP) at 150 MPa for 10 min. A highly dense sintered body was obtained after the sintering process at 1100 °C for 5 h, and it was confirmed to have a relative density of approximately 98% through the Archimedes' method.

Membrane Fabrication: A single-phase BLCFN perovskite membrane was fabricated using the tape-casting method. A slurry for tape casting was prepared by blending the appropriate amounts of binder, n-propyl acetate, ethanol, dispersant, and plasticizer.[66] After ball-milling the slurry for 48 h, additional defoaming was performed. The slurry was applied to the carrier film of the tape caster and the thickness of the green sheet was adjusted using a doctor blade. It was confirmed that the tape-casted green sheet had a uniform thickness of approximately 30 μm. To control the thickness of the membrane, the green sheets were laminated at 70 °C under a pressure of 430 bar using a warm isostatic press. The laminated tape was sintered at 1000 °C for 6 h to densify the membrane, and the relative density determined by Archimedes' method showed 97% of the theoretical density. To improve the surface exchange reaction, a BLCFN active layer was coated uniformly to both ends of the sintered membrane using a brush painting method, followed by heat treatment at 900 °C for 3 h. The oxygen permeation flux of the membrane was analyzed using a zirconia gas sensor and gas chromatograph (ACME 6000, YoungLin, Korea). The BLCFN membrane was positioned on an alumina tube and sealed using a glass sealant to maintain the oxygen partial pressure difference across the membrane. For the oxygen permeation tests, synthetic air (21 vol% O_2 and 79 vol% N_2) was employed as the feed gas, while high-purity helium gas (99.999%) served as the permeate gas. The flow rate was regulated using a mass flow meter. The oxygen permeation flux was determined by measuring the oxygen concentration in the effluent gas. In this study, the concentration of N_2 present in the effluent gas was less than 1%, indicating that the impact of gas leakage was negligible.

Oxygen Nonstoichiometry and Electrical Conductivity: A series of experiments were conducted to determine the oxygen nonstoichiometry ($\delta = \Delta\delta + \delta^*$) of BLCFN. Firstly, thermogravimetric analysis (TGA) and coulometric titration were employed to measure $\Delta\delta$ as a function of temperature and oxygen partial pressure. In addition, δ^* was determined via iodometric titration. The laboratory-made TGA system, featuring the Cahn D200 microbalance, is designed to ensure exceptional precision in measurements by carefully considering a myriad of error sources stemming from the demanding high-temperature conditions, such as thermal convection flow, electrostatic effects, thermal diffusion, radiation effects, buoyancy, thermomolecular flow, and aerodynamic effects.[67–69] This TGA system exhibits a resolution of ±0.5–1.5 μg within a wide range of oxygen partial pressures and up to approximately 1000 °C in temperature. Further details can be found in literature.[69]

The measured weight change, Δw, was converted into relative oxygen nonstoichiometry ($\Delta\delta$) using the following equation

$$\Delta\delta = \frac{M_{\text{Sample}}}{M_O}\frac{\Delta w}{w_s} \quad (55)$$

where, w_s, M_{sample}, and M_O are the initial weight, molar weight, and atomic oxygen, respectively. The configuration of the galvanic cell used for the coulometric titration is as follows

$$aO_2, \text{ Specimen} \mid \text{YSZ} \mid aO_2 \quad (56)$$

The oxygen pumped out from the specimen over a certain period of time through solid electrolyte in galvanostatic mode includes not only the oxygen from the specimen but also the gas in the enclosed space of the galvanic cell; thus, relative oxygen nonstoichiometry ($\Delta\delta$) is as follows

$$\Delta\delta = \delta - \delta^* = \left(\frac{It}{2F} - \frac{2V_d}{RT}\Delta P_{O_2(g)}\right)\frac{M}{m_o} \quad (57)$$

where I, t, F, R, T, V_d, m_O, and M represent the current, time, Faraday constant, gas constant, temperature, dead volume in the electrochemical cell, weight of the specimen, and molar mass of the specimen, respectively. The equilibrium oxygen partial pressure, $\Delta P_{O_2(g)}$, inside the cell is calculated using the Nernst equation.

$$a_{O_2} = a_{O_2}^{ref} \exp\left(\frac{4FE}{RT}\right) \quad (58)$$

Considering the geometric factors of the yttria-stabilized zirconia (YSZ) electrolyte and the specimen used in the titration cell, the error due to the leakage current was calculated to be approximately 1% when the ratio of $a_{O_2}^{ref}/a_{O_2}^{in}$ was in the range of $10^0 \approx 10^{-4}$.

For idometric titration, the powder was dissolved in 6 N HCl and distilled water with 20 mL of potassium iodide (KI, Alfa Aesar) solution as the color indicator and starch. Subsequently, the solution was titrated with a 0.025 N sodium thiosulfate solution ($Na_2S_2O_3$, Daechung).

Electrical conductivity and conductivity relaxation measurements were performed by the DC 4-probe method using bar-type specimens with dimensions of $3 \times 3 \times 16\,mm^3$. A constant current source (Keithley 6220) was used, and the conductivity was calculated from the slope of the voltage with respect to the current. In the conductivity relaxation experiments, a 4-way valve was used to change the oxygen partial pressure surrounding the specimens rapidly under isothermal conditions. The oxygen partial pressure was controlled and monitored using a digital multimeter (Keithley 2700), digital gas flow controller (MFC), and ex-situ YSZ electrochemical oxygen sensor.

Iso/Non-Isothermal Electrochemical Blocking Cell: The design of the electrochemical polarization cell incorporated several considerations to ensure accurate measurements. These considerations include the utilization of in situ ion and electron probes for measuring ionic and electronic fluxes, a small driving force to comply with the Onsager reciprocal relation, the inhibition of mass exchange at the solid–gas interface except for the measurement area, and the consideration of chemical reactions between the components of the electrochemical cell during prolonged high-temperature operation.

For the isothermal electrochemical cell, a cuboidal green specimen was molded and subjected to cold isostatic pressing. The resulting specimen was then heat-treated at 800 °C in air for 2 h. Four circular holes were drilled at specific locations to accommodate ion and electron probes. YSZ was selected as the ion probe, and a Pt wire was used as the electron probe. The electron probe was placed vertically at the same location as the ion probe. After the sintering process (1100 °C, 5 h), a reversible electrode was constructed on one side of the specimen in the c-axis direction. On the opposite side, an ion-blocking electrode was formed by attaching a 1 mm thick YSZ disk using a Pt paste. YSZ acts as a blocking barrier against the surrounding oxygen gas, allowing the measurement of the oxygen chemical potential of the specimen. A glass-based sealant (Aremco Ceramabind 643-2) was used in the final step. After drying at room temperature for 1–2 h, the sealing material underwent a curing process at specific temperatures: 93 °C for 2 h, 177 °C for 1 h, and 260 °C for 1 h, ultimately achieving a final and effective seal. Considering the complex cell configuration, the temperature was controlled with a slow heating rate of 1 °C min^{-1}. In addition, a thermocouple was positioned near the specimen for in-situ temperature measurements.

In the non-isothermal polarization experiments, the Soret effect induced by temperature gradients was measured in a closed system without any mass exchange with the surroundings. Therefore, the YSZ ion-blocking electrodes were symmetrically configured at both ends of the sintered specimens. The Pt gauze with Pt-Rd(10%)/Pt wire was positioned on the specimen–YSZ interface and the outer surface of YSZ and then thermally bonded using Pt paste at 900 °C for 2 h. A glass-based sealant (Aremco Ceramabind 643-2) was coated on the other surfaces of the specimen. A temperature gradient was applied to the electrochemical cell by introducing a local heater beneath it.

Thermal Expansion: The thermal expansion coefficient (TEC) was measured using a dilatometer (Netzch L75 PT160 dilatometer). The sintered specimens were carefully loaded into the dilatometer, and measurements were taken while ramping up the temperature from room temperature to 1000 °C at a heating rate of 3 °C min^{-1}. After completing the experiment, the values were calibrated using an alumina rod under the same experimental conditions.

Supporting Information

Supporting Information is available from the Wiley Online Library or from the author.

Acknowledgements

H.B. and G.D.N. contributed equally to this work. This work was supported by Korea Electric Power Corporation (grant no. R18XA06-77), National Research Foundation of Korea (NRF) grant funded by the Korea government (MSIT) (grant no. 2018R1A5A1025224), and National Research Foundation of Korea (NRF) grant funded by the Korea government (MSIT) (grant no. 2022R1A2B5B02001873).

Conflict of Interest

The authors declare no conflict of interest.

Data Availability Statement

The data that support the findings of this study are available from the corresponding author upon reasonable request.

Keywords

$Ba_{0.95}La_{0.05}Co_{0.8}Fe_{0.12}Nb_{0.08}O_{3-\delta}$, mass/charge transport properties, oxygen permeability, oxygen permeation membrane

Received: February 28, 2024
Revised: April 22, 2024
Published online: June 3, 2024

[1] Y. Teraoka, H. M. Zhang, K. Okamoto, N. Yamazoe, *Mater. Res. Bull.* **1988**, *23*, 51.
[2] J. H. Park, Y.-I. Kwon, G. D. Nam, J. H. Joo, *J. Mater. Chem. A* **2018**, *6*, 14246.
[3] W. Liang, S. K. Megarajan, F. Liang, Y. Zhang, G. He, Z. Liu, H. Jiang, *Chem. Eng. J.* **2016**, *305*, 176.
[4] Z. Wang, Z. Li, Y. Cui, T. Chen, J. Hu, S. Kawi, *Environ. Sci. Technol.* **2019**, *53*, 9937.
[5] S. Baumann, J. M. Serra, M. P. Lobera, S. Escolástico, F. Schulze-Küppers, W. A. Meulenberg, *J. Membr. Sci.* **2011**, *377*, 198.
[6] S. Engels, F. Beggel, M. Modigell, H. Stadler, *J. Membr. Sci.* **2010**, *359*, 93.
[7] R. Kiebach, S. Pirou, L. Martinez Aguilera, A. B. Haugen, A. Kaiser, P. V. Hendriksen, M. Balaguer, J. García-Fayos, J. M. Serra, F. Schulze-Küppers, M. Christie, L. Fischer, W. A. Meulenberg, S. Baumann, *J. Mater. Chem. A* **2022**, *10*, 2152.
[8] C. Wagner, *Prog. Solid State Chem.* **1975**, *10*, 3.
[9] Y. Cheng, H. Zhao, D. Teng, F. Li, X. Lu, W. Ding, *J. Membr. Sci.* **2008**, *322*, 484.
[10] J. Yi, J. Brendt, M. Schroeder, M. Martin, *J. Membr. Sci.* **2012**, *387–388*, 17.
[11] T. Kida, D. Takauchi, K. Watanabe, M. Yuasa, K. Shimanoe, Y. Teraoka, N. Yamazoe, *J. Electrochem. Soc.* **2009**, *156*, E187.
[12] Z. Qiu, Y. Hu, X. Tan, S. S. Hashim, J. Sunarso, S. Liu, *Chem. Eng. Sci.* **2018**, *177*, 18.
[13] Y. Lu, H. Zhao, X. Cheng, Y. Jia, X. Du, M. Fang, Z. Du, K. Zheng, K. Wierczek, *J. Mater. Chem. A* **2015**, *3*, 6202.

[14] K. Watenabe, M. Yuasa, T. Kida, Y. Teraoka, N. Yamazoe, K. Shimanoe, *Adv. Mater.* **2010**, *22*, 2367.
[15] H. Bae, B. Singh, L. Mathur, J. H. Joo, S.-J. Song, *J. Electrochem. Soc.* **2021**, *168*, 034511.
[16] T. Lee, D. Y. Cho, H. S. Kwon, H. I. Yoo, *Phys. Chem. Chem. Phys.* **2015**, *17*, 2598.
[17] C. Chen, D. Chen, Y. Gao, Z. Shao, F. Ciucci, *J. Mater. Chem. A* **2014**, *2*, 14154.
[18] P. Shen, X. Liu, H. Wang, W. Ding, *J. Phys. Chem. C* **2010**, *114*, 22338.
[19] X. Tang, X. Zhang, W. Luo, C. Wu, Y. Zhang, W. Ding, C. Sun, *J. Mater. Sci.* **2016**, *51*, 3971.
[20] H. Hu, Y. Lu, X. Zhou, J. Li, X. Wang, X. Ding, *J. Power Sources* **2022**, *548*, 232049.
[21] X. Zhou, M. Li, W. Yang, H. Hu, J. Li, Y. Lu, X. Wang, X. Ding, *Electrochim. Acta* **2022**, *425*, 140697.
[22] D. R. Lide, G. Baysinger, L. I. Berger, R. N. Goldberg, H. V. Kehiaian, K. Kuchitsu, D. L. Roth, D. Zwillinger, *CRC Handbook of Chemistry and Physics Editor-in-Chief, Section 9*, CRC Press LLC, Boca Raton, FL **2015**, p. 53.
[23] J. Wang, M. Saccoccio, D. Chen, Y. Gao, C. Chen, F. Ciucci, *J. Power Sources* **2015**, *297*, 511.
[24] X. Ding, X. Gao, W. Zhu, J. Wang, J. Jiang, *Int. J. Hydrogen Energy* **2014**, *39*, 12092.
[25] B. J. Kim, E. Fabbri, D. F. Abbott, X. Cheng, A. H. Clark, M. Nachtegaal, M. Borlaf, I. E. Castelli, T. Graule, T. J. Schmidt, *J. Am. Chem. Soc.* **2019**, *141*, 5231.
[26] G. D. Nam, Y.-I. Kwon, S. W. Lee, T. Ho Shin, J. H. Joo, *Sep. Purif. Technol.* **2023**, *318*, 123919.
[27] J. M. Serra, J. Garcia-Fayos, S. Baumann, F. Schulze-Küppers, W. A. Meulenberg, *J. Membr. Sci.* **2013**, *447*, 297.
[28] S. Y. Jeon, H. N. Im, B. Singh, M. Choi, Y. S. Yoo, J. H. Hwang, S. J. Song, *Ceram. Int.* **2015**, *41*, 7446.
[29] X. Meng, W. Ding, R. Jin, H. Wang, Y. Gai, F. Ji, Y. Ge, D. Xie, *J. Membr. Sci.* **2014**, *450*, 291.
[30] K. Watanabe, M. Yuasa, T. Kida, K. Shimanoe, Y. Teraoka, N. Yamazoe, *Solid State Ionics* **2008**, *179*, 1377.
[31] H. J. M. Bouwmeester, H. Kruidhof, A. J. Burggraaf, *Solid State Ionics* **1994**, *72*, 185.
[32] G. D. Nam, G. Lee, S. Choi, J. Lee, S. J. Song, J. H. Joo, *J. Mater. Chem. A* **2020**, *8*, 23884.
[33] Y.-I. Kwon, G. D. Nam, G. Lee, S. Choi, J. H. Joo, *Adv. Energy Sustainability Res.* **2022**, *3*, 2200086.
[34] Y.-I. Kwon, J. H. Park, S. M. Kang, G. D. Nam, J. W. Lee, J. H. Kim, D. Kim, S. M. Jeong, J. H. Yu, J. H. Joo, *Energy Environ. Sci.* **2019**, *12*, 1358.
[35] Y. Zhu, W. Li, X. Zhu, W. Yang, *AICHE J.* **2017**, *63*, 4043.
[36] C. Zhang, Y. Zhu, X. Wang, Y. Huang, L. Zeng, K. Li, P. Yu, K. Wang, L. Li, Z. Xiang, R. Chen, X. Zhu, H. Luo, *J. Membr. Sci.* **2024**, *696*, 122485.
[37] E. Bucher, A. Egger, P. Ried, W. Sitte, P. Holtappels, *Solid State Ionics* **2008**, *179*, 1032.
[38] A. Berenov, A. Atkinson, J. Kilner, M. Ananyev, V. Eremin, N. Porotnikova, A. Farlenkov, E. Kurumchin, H. J. M. Bouwmeester, E. Bucher, W. Sitte, *Solid State Ionics* **2014**, *268*, 102.
[39] T. Lee, H. S. Kim, H. I. Yoo, *Solid State Ionics* **2014**, *262*, 2.
[40] E. D. Eastman, *J. Am. Chem. Soc.* **1926**, *48*, 1482.
[41] H. I. Yoo, H. Schmalzried, H. Martin, J. Janek, *Z. Phys. Chem.* **1990**, *168*, 129.
[42] C. Wagner, *Prog. Solid State Chem.* **1972**, *7*, 1.
[43] A. D. LeClaire, *Phys. Rev.* **1954**, *93*, 344.
[44] K. C. Lee, H. I. Yoo, *J. Phys. Chem. Solids* **1999**, *60*, 911.
[45] J.-H. Park, R. N. Blumenthal, *J. Electrochem. Soc.* **1989**, *136*, 2867.
[46] H.-I. Yoo, S.-H. Park, J. Chun, *J. Electrochem. Soc.* **2010**, *157*, B215.
[47] M. B. Choi, D. K. Lim, E. D. Wachsman, S. J. Song, *Solid State Ionics* **2012**, *221*, 22.
[48] M.-B. Choi, S.-Y. Jeon, H.-N. Im, E. D. Wachsman, S.-J. Song, *J. Electrochem. Soc.* **2011**, *159*, P23.
[49] J. Song, D. Ning, H. J. M. Bouwmeester, *Phys. Chem. Chem. Phys.* **2020**, *22*, 11984.
[50] H. Bae, B. Singh, I.-H. Kim, H.-N. Im, S.-J. Song, *J. Electrochem. Soc.* **2018**, *165*, F641.
[51] H. Bae, J. Hong, B. Singh, A. K. Srivastava, J. H. Joo, S.-J. Song, *J. Electrochem. Soc.* **2019**, *166*, F180.
[52] J. Yoo, C. Y. Park, A. J. Jacobson, *Solid State Ionics* **2004**, *175*, 55.
[53] T. Ishigaki, S. Yamauchi, K. Kishio, J. Mizusaki, K. Fueki, *J. Solid State Chem.* **1988**, *73*, 179.
[54] C. H. Chen, H. J. M. Bouwmeester, R. H. E. Van Doom, H. Kruidhof, A. J. Burggraaf, *Solid State Ionics* **1997**, *98*, 7.
[55] W. Wagner, K. M. De Reuck, R. Schmidt, J. Ewers, R. B. Stewart, R. T. Jacobsen, *Oxygen, International Thermodynamic Tables of the Fluid State*, Vol. *9*, Blackwell Scientific Publications, Oxford **1987**, pp. 30–35
[56] C. Korte, J. Janek, *J. Phys. Chem. Solids* **1997**, *58*, 623.
[57] J. Janek, C. Korte, *Solid State Ionics* **1996**, *92*, 193.
[58] D. Shin, H. I. Yoo, *Phys. Chem. Chem. Phys.* **2017**, *19*, 11120.
[59] J. Mizusaki, T. Sasamoto, W. R. Cannon, H. K. Bowen, *J. Am. Ceram. Soc.* **1982**, *65*, 363.
[60] T. Nakamura, K. Yashiro, K. Sato, J. Mizusaki, *J. Solid State Chem.* **2009**, *182*, 1533.
[61] J. Mizusaki, S. Yamauchi, K. Fueki, A. Ishikawa, *Solid State Ionics* **1984**, *12*, 119.
[62] J. Mizusaki, Y. Mima, S. Shigeru, Y. And, K. Fuekir, *J. Solid State Chem.* **1989**, *80*, 102.
[63] T. Nakamura, H. Gao, K. Ohta, Y. Kimura, Y. Tamenori, K. Nitta, T. Ina, M. Oishi, K. Amezawa, *J. Mater. Chem. A* **2019**, *7*, 5009.
[64] A. S. Harvey, F. J. Litterst, Z. Yang, J. L. M. Rupp, A. Infortuna, L. J. Gauckler, *Phys. Chem. Chem. Phys.* **2009**, *11*, 3090.
[65] J.-I. Jung, S. T. Misture, D. D. Edwards, *Solid State Ionics* **2012**, *206*, 50.
[66] K. S. Yun, Y.-I. Kwon, J. H. Kim, S. Jo, C. Y. Yoo, J. H. Yu, J. H. Joo, *J. Eur. Ceram. Soc.* **2016**, *36*, 1835.
[67] R. Dieckmann, *Ber. Bunsen Ges. Phys. Chem.* **1982**, *86*, 112.
[68] W. Kuhn, E. Robens, G. Sandstede, G. Walter, *Vac. Microbalance Tech.* **1970**, *10*, 161.
[69] M. B. Choi, S. Y. Jeon, H. N. Im, S. J. Song, *J. Alloys Compd.* **2012**, *513*, 487.
[70] J. W. Stevenson, T. R. Armstrong, R. D. Carneim, L. R. Pederson, W. J. Weber, *J. Electrochem. Soc.* **1996**, *143*, 2722.
[71] H. Wang, Y. Cong, W. Yang, *J. Membr. Sci.* **2002**, *210*, 259.
[72] R. H. van Doorna, I. C. Fullartonb, R. A. de Souzab, J. A. Kilnerb, H. J. Bouwmeestera, A. J. Burggraaf, *Solid State Ionics* **1997**, *96*, 1.